INTERNATIONAL JOURNAL FOR NUMERICAL METHODS IN FLUIDS
Int. J. Numer. Meth. Fluids 2005; **47**:99–120
Published online 25 November 2004 in Wiley InterScience (www.interscience.wiley.com). DOI: 10.1002/fld.781

Large eddy simulations of turbulent swirling flows in a dump combustor: a sensitivity study

P. Wang and X. S. Bai*,†

Division of Fluid Mechanics, Lund Institute of Technology, S-221 00 Lund, Sweden

SUMMARY

Large eddy simulations (LES) of confined turbulent swirling flows in a model dump combustor are carried out. The simulations are based on a high-order finite difference method on a Cartesian grid, with the sub-grid scale stress tensor modelled using a scale-similarity model. The aims of this work are to study the physics of the flow and to evaluate the performance of LES method for simulation of the major features of turbulent swirling flows—the vortex breakdown, the highly anisotropic and fast-decaying turbulence structure. Influences of inflow/outflow conditions, combustor geometry, inlet swirl profile and Reynolds numbers on the vortex breakdown and turbulence structures are investigated. At very high swirl levels, the influence of the outflow conditions and the outlet geometry is fairly significant, not only at downstream near the outlet, but also at far upstream. At low Reynolds numbers, the onset of vortex breakdown is fairly sensitive to the change of Reynolds number; however, at high Reynolds numbers it is rather insensitive to the Reynolds number. Comparisons of LES results with experimental data are made. The LES results are shown to be in reasonably good agreement with the experimental data if appropriate inflow and outflow boundary conditions are imposed. Copyright © 2004 John Wiley & Sons, Ltd.

KEY WORDS: swirling flow; large eddy simulation; internal recirculation zone; vortex breakdown; boundary conditions

1. INTRODUCTION

Turbulent swirling flows are of great importance in practical applications, for example in aeronautics, heat transfer, combustion and separation devices. They have attracted extensive research efforts for decades. Experimental [1, 2], theoretical [3, 4] and numerical [5–7] investigations of swirling flows have been reported. Previous studies showed that an internal recirculation zone (IRZ), which is often referred to as vortex breakdown phenomenon in fluid

*Correspondence to: X. S. Bai, Division of Fluid Mechanics, Lund Institute of Technology, S-221 00 Lund, Sweden.
†E-mail: xue-song.bai@vok.lth.se

Contract/grant sponsor: Swedish Research Council (VR)
Contract/grant sponsor: Center for Combustion Science and Technology (CeCOST)
Contract/grant sponsor: National Supercomputer Center (NSC)

Received 16 November 2003
Revised 22 June 2004

mechanics, appears, when the strength of swirl is high enough. In combustion systems, IRZ serves as a reservoir of heat and radicals that re-ignite the reactant mixture and thereby stabilize the flame. IRZ affects the flame shape, flame stability and heat release rate, as well as emission of nitrogen oxide [8]. Development and improvement of modern gas turbine combustion chambers demand a deeper understanding of the fundamental physics and appropriate numerical simulations of turbulent swirling flows.

In swirling flows large velocity gradients exist; the flow structure is highly anisotropic. It has been shown that the k–ε turbulence model is inadequate for simulation of strong swirling flows [5, 6]. This is due to the fact that the k–ε turbulence model is based upon the Boussinesq hypothesis; it does not take into account the effect of the rotational motion. Weber *et al.* [7] tested three turbulence models in a simulation of confined turbulent swirling flows: a k–ε model, a Reynolds stress model (RSM) and an algebraic stress model (ASM). It was shown that RSM and ASM perform better than the k–ε model. Modification of RSM simulations of swirling flows has been attempted recently. For example, Lu and Semião [9] showed successful simulations of confined swirling flows by using an improved RSM model, in which an anisotropic dissipation rate model was used for calculation of turbulent kinetic energy and a non-linear model for the pressure–strain correlation.

Large eddy simulation (LES) provides an effective tool for handling complex turbulent flows. It has several advantages over those turbulence models within the Reynolds-averaged Navier–Stokes (RANS) framework. LES needs only to model small-scale eddies that are not supported by the spatial filter. Since the small eddies contain less turbulent kinetic energy, have a more universal behaviour and are more isotropic, it is relatively easier to model them. LES can resolve all eddies in turbulence and becomes direct numerical simulation (DNS), if the grid resolution is high enough. Another important feature of LES is its ability of capturing the unsteady motion that may be important in turbulent swirling flows. Unsteady motion of coherent, non-turbulent structures can occur at high swirl numbers—which is known as the 'precessing vortex core (PVC)' [10]. Correct simulation of the PVC location and the frequencies of the PVC shedding is important for the combustor design and for preserving the combustion stability. Most previous LES have been focused on the so-called 'building-block' flows such as channel flows, boundary layer flows or free-jet flows [11]. Application of LES to simulation of turbulent swirling flows has recently attracted the attention of many researchers [12, 13].

LES requires a time-dependent turbulent inflow condition since the simulated turbulent flow is time dependent. Such a 'turbulent inflow condition' is often absent from the measurements. It must be generated in other numerical simulations or presumed following certain but limited measurement data. Many inflow boundary conditions have been proposed and tested [14–16]. A simple method is to start the calculation with a laminar flow profile (without turbulent fluctuations); it evolves into 'realistic' turbulence after some distance downstream. This implies that the inlet must be located far away from the region of interest. An alternative way is to add some kind fluctuations to the laminar profile, for example white noise with certain scaling. More accurate turbulent inflow conditions can be obtained from an auxiliary simulation [17] or by use of periodic boundary conditions [16]. The simulated instantaneous flow velocity is stored as a 'library' to be used, with proper re-scaling, as the inflow condition of later LES. Klein *et al.* [14] presented a novel approach for generating artificial velocity data which reproduces the first- and the second-order one point statistics as well as a locally given auto-correlation function.

Similar to the inflow condition, outflow condition is also important for LES. In order to eliminate the influence of errors due to the outflow condition on the upstream flow, the outlet should be put far away from the region of interest. Due to the limitation of computing resource, it is not always easy to fulfil this requirement.

An often used outflow condition is the zero-gradient condition, i.e. the gradient of the dependent variables in the normal direction to boundary is set to zero. This condition is appropriate if the outflow has a fully developed self-similar profile. In References [17, 18], another outflow condition, a 'convective outflow' boundary condition, has been applied in the numerical calculation of incompressible turbulent flow. It was found that the convective outflow condition allows the vortical structures to move out the domain with minimum distortion.

In this work, we examine the performance of LES for simulation of turbulent swirling flows in a dump combustor configuration. The focus of this paper is on assessing the influence of the inflow and outflow boundary conditions as well as other geometrical and flow parameters on swirling flow simulations. Three inflow conditions (the 'laminar inflow', the random fluctuation and the re-scaled inflow library condition) and two outflow conditions (the zero-gradient and the convective outflow condition) are tested. The influences of these conditions on the mean flow field, the variance and the turbulent kinetic energy distributions are explored. Further, we investigate the influence of the inflow swirl profile, the combustor length and the Reynolds number on the turbulence and the vortex breakdown structures.

2. NUMERICAL METHODS AND SUB-GRID SCALE (SGS) MODEL

The employed governing partial differential equations (PDE) for a turbulent isothermal swirling flow are the Navier–Stokes equations for incompressible flows. This set of governing equations is appropriate for low Mach number flows. The numerical simulations are based on a so-called Cartesian grid method developed previously [19]. The basic idea is to use the Cartesian grid for obtaining a high-order numerical discretization of the governing PDE, and to minimize the filter/finite difference commutation errors. In order to overcome the shortcoming of Cartesian grid in dealing with curve wall boundaries, a high-order accuracy wall algorithm [19] is used.

2.1. Governing equations

In the Cartesian co-ordinate system, the governing equations for isothermal incompressible viscous flows can be written as:

$$\frac{\partial u_j}{\partial x_j} = 0 \tag{1}$$

$$\frac{\partial u_i}{\partial t} + \frac{\partial u_i u_j}{\partial x_j} = -\frac{1}{\rho}\frac{\partial P}{\partial x_i} + \nu \frac{\partial^2 u_i}{\partial x_j^2} \tag{2}$$

Here t is time, ρ is the density, ν is the kinematic viscosity, and u_i $(i = 1, 2, 3)$ are the velocity components in Cartesian co-ordinate x_i directions, respectively. In the above equations, Einstein summation convention is used.

In LES, the flowfield is divided into large eddies that are fully resolved, and small eddies that have to be modelled. Due to the universal character of the small eddies, it is believed

that the small eddies are easier to model than those large eddies. A filter function G with the filter width Δ is applied to a flow variable ϕ to obtain a filtered flow variable $\bar{\phi}$, according to

$$\bar{\phi}(x,t;\Delta)=\int_{-\infty}^{+\infty} G(x-x';\Delta)\,\phi(x',t)\,\mathrm{d}x' \tag{3}$$

Applying this filtering procedure, the governing equations (1) and (2) can be written as:

$$\frac{\partial \bar{u}_j}{\partial x_j}=0 \tag{4}$$

$$\frac{\partial \bar{u}_i}{\partial t}+\frac{\partial \bar{u}_i\bar{u}_j}{\partial x_j}=-\frac{1}{\rho}\frac{\partial \bar{P}}{\partial x_i}+\nu\frac{\partial^2 \bar{u}_i}{\partial x_j^2}-\frac{\partial \tau_{ij}}{\partial x_j} \tag{5}$$

A term τ_{ij} is introduced into the filtered momentum equation (5). It is the so-called SGS stress tensor, defined according to $\tau_{ij}=\overline{u_iu_j}-\overline{u_i}\,\overline{u_j}$. The SGS stress tensor cannot be expressed by the resolved variables because it consists of unknown terms, $\overline{u_iu_j}$. Many models for the SGS stresses have been proposed and tested in the literature [11]. One of the first models for the SGS tensor is the eddy viscosity-based model proposed by Smagorinsky [20]. A scale-similarity model (SSM) is used in this work.

2.2. SSM

SSM is based upon the assumption of a similar behaviour between the resolved stress and the unresolved one. The resolved stress is calculated by applying a second filtering procedure to the resolved variables. The SGS stress is then estimated by the resolved one. In this work, the SSM proposed by Liu *et al.* [21] is used. For incompressible isothermal flow, the model has the form:

$$\tau_{ij}=\widehat{\bar{u}_i\bar{u}_j}-\hat{\bar{u}}_i\hat{\bar{u}}_j \tag{6}$$

The filter function and the filter width of the additional filter applied in SSM have to be defined. The width of the second filter $\hat{\Delta}$ must be wider than Δ. In our simulations, the width of the second filter is twice the grid filter width, i.e. $\hat{\Delta}/\Delta=2$. Applying the second filter to the resolved quality, $\hat{\bar{\phi}}$ can be written as:

$$\hat{\bar{\phi}}(x,t;\hat{\Delta})=\int_{-\infty}^{+\infty} G(x-x';\hat{\Delta})\bar{\phi}(x',t;\Delta)\,\mathrm{d}x' \tag{7}$$

An approximate explicit Gaussian filter has been used in this work. In uniform Cartesian grid it is written as:

$$\hat{\bar{\phi}}=A\begin{pmatrix}\phi_{i-1}^{**}\\ \phi_i^{**}\\ \phi_{i+1}^{**}\end{pmatrix},\quad A=\frac{1}{6}(1\ \ 4\ \ 1),\quad \phi_i^{**}=A\phi_i^{*}A^{\mathrm{T}} \tag{8}$$

$$\phi_i^* = \begin{pmatrix} \bar{\phi}_{i,j-1,l-1} & \bar{\phi}_{i,j-1,l} & \bar{\phi}_{i,j-1,l+1} \\ \bar{\phi}_{i,j,l-1} & \bar{\phi}_{i,j,l} & \bar{\phi}_{i,j,l+1} \\ \bar{\phi}_{i,j+1,l-1} & \bar{\phi}_{i,j+1,l} & \bar{\phi}_{i,j+1,l+1} \end{pmatrix} \tag{9}$$

2.3. Numerical methods

The governing equations are discretized on a staggered Cartesian grid system with local grid refinements on the flow domain of high interest. Cartesian grid describes a curved boundary only approximately. In a low-order wall boundary treatment, a curve wall is represented by piecewise step-walls. Gullbrand *et al.* [19] developed a high-order wall algorithm, in which the uniform grid is kept at the wall, with the wall boundary condition being fulfilled at the exact wall location by using an interpolation and extrapolation procedure of the dependent variables.

The time integration is performed with a three-level, second-order implicit scheme. All spatial terms in the governing equations are discretized with a fourth-order central difference scheme, except the convective terms in the momentum equations, which are discretized using a third-order upwind scheme. Multi-Grid method is used to accelerate the convergence in each time step. More details of the numerical scheme can be found in Reference [19].

3. VALIDATION OF THE NUMERICAL METHODS

To validate the above numerical methods for simulation of swirling flows, an experimental test case [22] is selected, as described below.

3.1. Experiment test case

Figure 1 shows schematically the experimental dump combustor geometry and the characteristic flowfield. The combustor geometry can be viewed as a simplified gas turbine combustion chamber, where swirl is introduced to increase the mixing rate and to stabilize the flame. Two-component laser Doppler velocimetry (LDV) measurements were made to obtain time-averaged mean velocity and Reynolds stresses in the combustor. The measurements were made as radial profiles at different axial positions between $-2.1H \leqslant x \leqslant 19.54H$, where $x = 0$ is placed at the backward-facing step, as shown in the figure. H is the height of the backward-facing step, $H = R_2 - R_1$.

In the literature, the degree of swirl is usually characterized by a non-dimensional number, the swirl number S. It is the ratio between the axial flux of the azimuthal momentum to the axial flux of the axial momentum multiplied by an equivalent combustor radius, R_1.

$$S = \int_0^R UWr^2 \,\mathrm{d}r \Big/ \left(R_1 \int_0^R U^2 r \,\mathrm{d}r \right) \tag{10}$$

Here R_1 is the inlet combustor radius and R is the local combustor radius.

Flows with different swirl numbers and Reynolds numbers were measured. In this work, the test case with swirl number $S = 0.43$ is employed to validate LES; hereafter, this test case is denoted as S43. LES on the same combustor with different swirl numbers ($S = 0$ and 0.33)

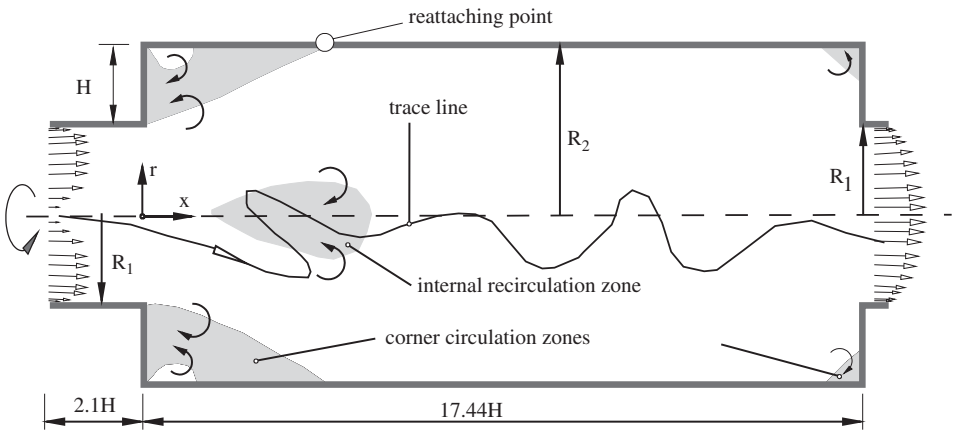

Figure 1. A sketch of the experimental test rig (S43). $R_1 = 25.32$ mm, $R_2 = 49.12$ mm, $H = 23.8$ mm. Shadow region shows recirculation zones.

Table I. Flow parameters of different tested cases.

Test cases	S	Re	U_b (m/s)	H/R_1	Comments
S43	0.43	20 000	2.72	0.94	Experiment test case
S43A	0.43	20 000	2.72	0.94	Inlet swirl different from S43
S43B	0.43	20 000	2.72	0.94	Inlet swirl different from S43
S65	0.65	21 000	6.558	0	Inlet swirl: solid body rotation
S180	1.8	21 000	6.558	0	Inlet swirl: solid body rotation
SRE	0.24–0.8	10^2–10^5	4.36	0.29	Inlet swirl: solid body rotation

had been performed. The results showed similar agreement with the experimental data as the case S43, thus, only results of S43 are presented below.

The swirl number in the experiments was evaluated at $x/H = -2.1$ (in the guiding pipe); in the immediate downstream of the backward-facing step (around $x/H = 1$) the swirl number is about 1. Flow parameters for test case S43 are given in Table I. The Reynolds number Re based on the inlet diameter and the inlet bulk velocity U_b is about 20 000. The characteristic turbulence intensity u' (root-mean-square of the velocity fluctuations, RMS) is estimated to be 10% of the U_b, the integral length scale l is in the order of H. Turbulent Reynolds number Re_l determined based on these quantities is about 940. Taylor micro-scale λ, estimated using $\lambda \sim l/\sqrt{Re_l}$, is about 0.776 mm. Taylor micro-scale represents the length scale in the inertial sub-range of the energy spectrum; it is desirable to resolve the Taylor micro-scale in LES.

The time-averaged mean axial, radial and azimuthal velocity profiles U, V, W obtained in the measurements at the axial position $x = -2.1H$ are used as the inflow condition. The inlet RMS velocity fluctuations u', v', w' are fulfilled by adding random-fluctuation to the mean velocity. The non-slip boundary condition is applied on the pipe wall. The zero-gradient outflow condition is used in the simulations, i.e. $\partial \bar{u}_i/\partial x = 0$ at the exit. Other inflow and outflow boundary conditions are tested in later sections.

3.2. Test of grid resolution

The computation domain is between $-2.1H \leqslant x \leqslant 17.44H$, which includes the contraction at the outlet. Three grid resolutions are tested, as shown in Table II. In order to improve the grid resolution and to keep the total grid points under an acceptable level, local refinements in all three co-ordinate directions are performed in Grid 2 and Grid 3 (see Table II). When using Grid 3, message passing interface (MPI) technique is used to parallelize the computation.

Figure 2 shows the time-averaged axial and azimuthal velocity components at different radial positions at the axial station $x/H = 2.1$. At this station, an IRZ and an annular recirculation zone are present. As seen, all three grids predict similar velocity profiles. Nevertheless, the influence of the grid resolution is evident. Grid 2 and Grid 3 yield a better agreement with the experimental data. The discrepancy between Grid 2 and Grid 3 is, however, not substantial. Considering the computational effort, Grid 2 is preferred. In the following analysis, computational results are obtained using Grid 2 (unless otherwise explicitly stated).

As noted from Figure 2, the azimuthal velocity profile differs considerably from the experimental data, which is not due to the grid resolution, but rather due to the use of the random fluctuation inflow condition. When a more realistic physical inflow condition is used, as shown in a later section, closer agreement with the experimental data is obtained.

Table II. Three grid resolutions have been tested.

Grid	Grid points (million)	Grid sizes (mm) $(x \times y \times z)$	Local refinement
1	2.1	$2.193 \times 1.196 \times 1.196$	No refinement
2	2.9	$1.973 \times 0.764 \times 0.764$	$x \leqslant 6H$
3	6.4	$1.292 \times 0.764 \times 0.764$	$x \leqslant 10H$

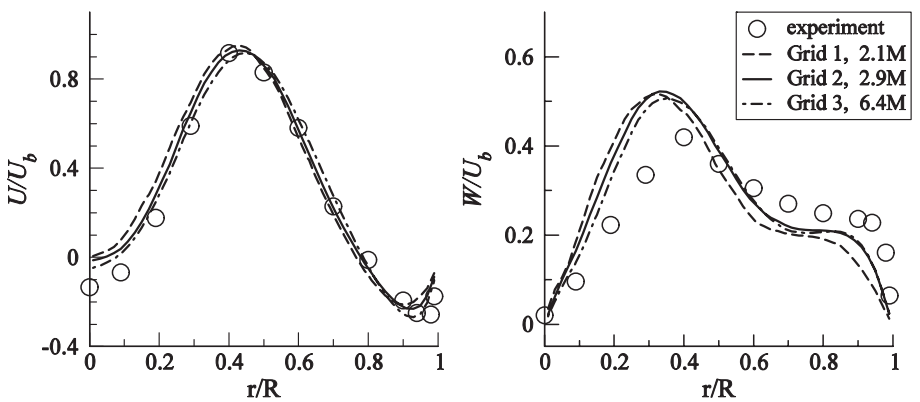

Figure 2. Radial profiles of the time-averaged axial and azimuthal velocity components by using different grid resolutions, $x/H = 2.1$, test case S43.

3.3. Comparisons with the experiments and discussion

Comparisons with the experimental data are shown in Figures 3 and 4. The time-averaged mean axial and azimuthal velocity profiles as well as the Reynolds stresses are plotted. The time-averaging calculation was performed using about 30 000 time steps, which was shown to give a converged time-average. The overall agreement between the experimental and the computational results is good.

As shown in Figure 3, due to the centrifugal force generated by the swirling motion, the center fluid is forced to move outward, and it results in a decrease of the axial velocity in the inner part near the axis and an increase in the outer part. Additionally, the sudden expansion at the backward-facing step wall introduces another axial velocity deceleration to the already low-speed flow at the axis centre of combustor. These two effects lead to the formation of an IRZ, as shown in the mean axial velocity profile, Figures 1–3.

Along the axial direction downstream, the axial and the azimuthal velocity profiles become smoother. At $x > 6.3H$, both the axial and the azimuthal velocity components are significantly lower than the peak values upstream, as shown in Figure 3. This is due to the high spreading rate of momentum in swirling flows. High spreading rate is an important property of swirling flows. In combustion systems it is often used to enhance the mixing of the reactants.

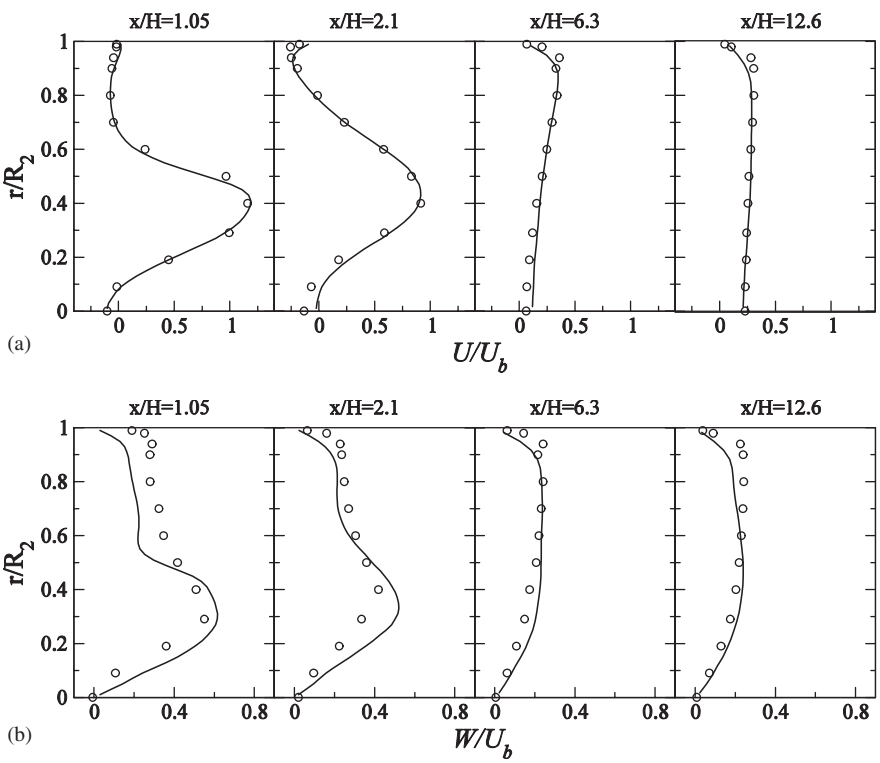

Figure 3. Radial profiles of the time-averaged axial and azimuthal velocity components at four axial positions of test case S43. Circle: experiment; solid line: computation.

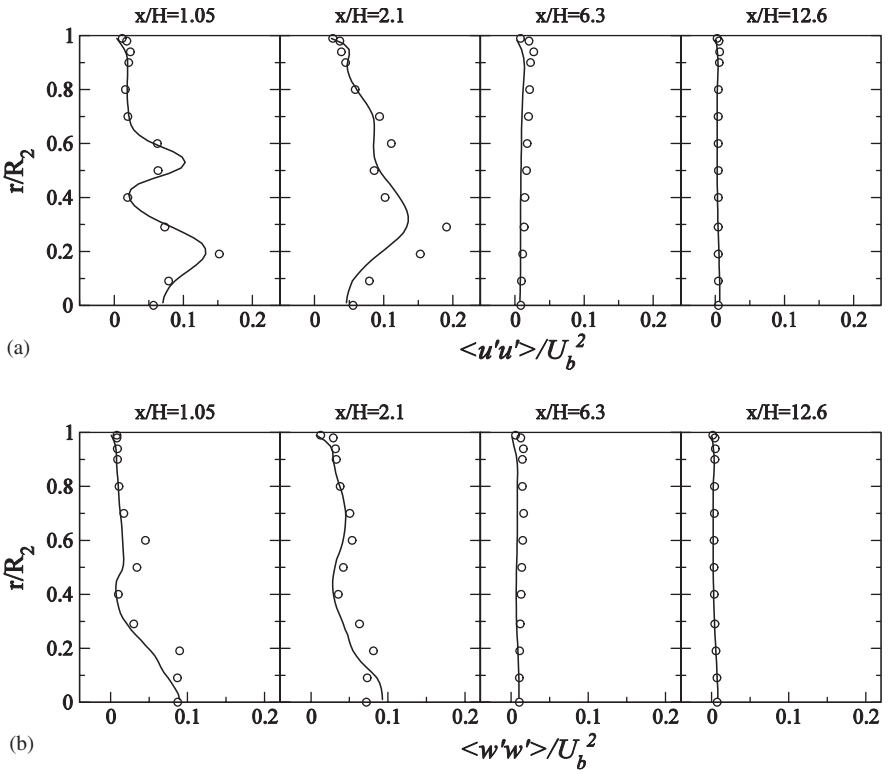

Figure 4. Radial profiles of the axial and azimuthal components of Reynolds stresses at four axial positions of test case S43. Circle: experiment; solid line: computation.

In Figure 4, the axial and azimuthal velocity components of the normal Reynolds stresses are plotted. At $x/H = 1.05$, two peaks are found in the profile of the axial stress component. These two peaks are formed due to the two strong shear layers in the flowfield—a shear layer near the shoulder of the backward-facing step wall and a shear layer caused by the IRZ. The latter shear layer locates at the boundary of the IRZ, where most of the turbulent kinetic energy is produced.

The axial and azimuthal components of Reynolds stresses differ significantly in the first few axial stations, which implies that turbulence in the region near the backward-facing step is highly anisotropic. It is shown that, after the recirculation zone, turbulence becomes isotropic quickly. It takes 5–6H downstream of the backward-facing step for the transition from anisotropic to rather isotropic turbulence. A similar result was reported in Reference [9]. In a non-swirl case with the same geometry, the transition took 12H (shown in the experimental data [22]). Additionally, in Figure 4 it is seen that the decay rate of turbulent fluctuation of swirling flow is high. After 6H downstream, the variances of the velocity components are almost negligible.

Discrepancy in the predicted peak values of the Reynolds stresses is seen in Figure 4. The peak axial stress from LES is lower than the experimental data. The peak azimuthal

Reynolds stresses from LES at $r/R = 0.6$ is about half of the measured one. This position is corresponding to the shear layer after the backward facing step. This discrepancy is possibly caused by the insufficient grid resolution at the shear layer and the poor inflow turbulence condition. The inflow turbulence is introduced by adding random-fluctuations to the mean velocity. This is a simple way to generate time-dependent inflow condition; however, due to the lack of physical correlation between different eddies, this artificial random fluctuation introduces a wrong turbulent kinetic energy transfer between different eddies. In the following sections, the impact of inflow and outflow boundary conditions is investigated.

4. SENSITIVITY OF SWIRLING FLOWS TO GEOMETRICAL AND FLOW PARAMETERS

4.1. Influence of inflow boundary conditions

In this section, three different inflow conditions are investigated: (1) a non-fluctuation, i.e. 'laminar inflow' condition; (2) a random-fluctuation condition (which is used in the previous section); and (3) a re-scaled inflow library condition.

Pierce [23] and Pierce and Moin [24] presented a so-called body force technique to create turbulence inflow conditions. An axial force is used to represent the mean pressure gradient that drives the main flow and an azimuthal body force is used to overcome the drag from the walls and drives the azimuthal flow. The method is applicable if the flow at the inlet is fully developed to turbulence. In the current experiments, a long guiding pipe (about $29H$) is employed to connect the swirl generator and the main test section. The flow is assumed to be fully developed to turbulence at the end of the guiding pipe. The body force method is used here to generate the inflow turbulence for the main test section. The LES data at the middle cross-section is stored to form a 'library' of the instantaneous velocity. The velocity library, then, is re-scaled to create the inlet flow instantaneous velocity that satisfies the measured statistics properties (the mean and the variances). For instance, if the original database from the velocity library u_{ori} has a mean value of U_{ori} and RMS velocity fluctuation of u'_{ori}, the re-scaled new inflow velocity u_{new} with a new mean value U_{new} and a new RMS velocity fluctuation u'_{new}, can be calculated as follows:

$$u_{\text{new}} = U_{\text{new}} + (u_{\text{ori}} - U_{\text{ori}}) \frac{u'_{\text{new}}}{u'_{\text{ori}}} \tag{11}$$

This inflow condition reproduces the measured Reynolds normal stresses and turbulent kinetic energy, but not the shear stresses. To obtain physically realistic statistics at the inflow, the inflow library should contain sufficient number of time steps. 10 000 time steps are used in this work. When the LES time step exceeds 10 000, the inflow library is repeated from the starting first time step.

The energy time spectra of the random-fluctuation and the re-scaled inflow library conditions are plotted in Figure 5. The random-fluctuation produces an almost constant distribution of turbulent kinetic energy over all the time (and length) scales. This is in contradicting with the well-known turbulent flow theory, i.e. the turbulent energy cascade that describes the energy transfer between large scales and small scales. Since the re-scaled inflow library condition is originated from the turbulent flow calculation, it has a more reasonable turbulent kinetic

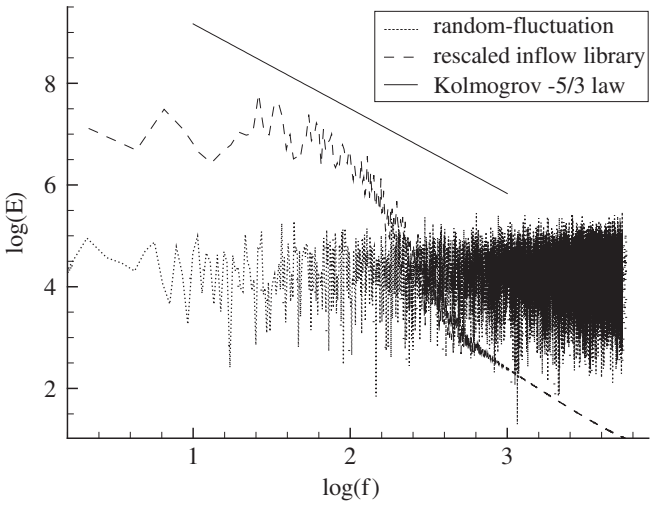

Figure 5. Eulerian energy time spectra of the random-fluctuation inflow and the re-scaled turbulent inflow library.

energy spectrum: most energy is contained in the large length scales (low frequency, f), and the turbulent kinetic energy becomes lower when the length scale decreases from the integral length scale. The Kolmogorov $-\frac{5}{3}$ power law in the inertial subrange is shown by a straight line.

The three inflow boundary conditions have been used to compute the same swirling flow, Case S43. The mean axial and azimuthal velocity profiles at two axial stations, $x/H = 1.05$ and 2.1, are plotted together with the experimental data in Figure 6. Two inflow conditions, the 'laminar inflow' condition and the random fluctuation condition predicted approximately the same maximum axial velocity and the peak position as the experimental data at $x/H = 1.05$. The re-scaled turbulent inflow library condition gave a little different axial velocity—at $x/H = 2.1$ the peak of the axial velocity is shifted towards the outer wall—this leads to a slightly different shape of IRZ. More significant difference between results from the three inflow conditions are seen in the azimuthal velocity profiles; the re-scaled turbulent inflow condition shows a much better agreement in the azimuthal velocity distribution. The 'laminar inflow' condition and the random-fluctuation inflow condition yield similar results that differ from the results obtained using the re-scaled turbulent inflow library condition. This shows that adding random fluctuations to the mean velocity profile is almost equivalent to not adding any fluctuations to the profile, which suggests that the random-fluctuation inflow condition is not adequate for LES of turbulent flows.

The influence of these inflow conditions can also be seen in the distribution of the mean turbulence kinetic energy along the axis of the combustor, as given in Figure 7. The 'laminar inflow' condition has a zero turbulent kinetic energy at the inlet port. With this inflow condition the turbulent kinetic energy increases continually from zero value to a peak at about $x/H = 1.5$, which is downstream of the measured location of the peak turbulent kinetic energy. Further downstream, turbulent kinetic energy decays very quickly, as also shown in Figure 4.

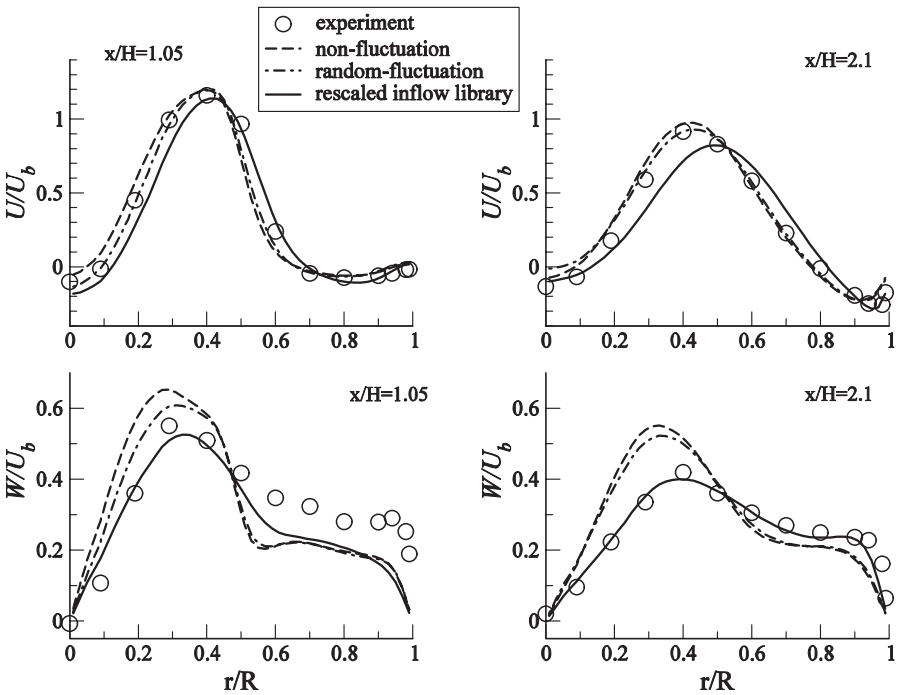

Figure 6. Radial profiles of the time-averaged axial and azimuthal velocity components at two axial positions of test case S43, from the experiment and LES using three different inflow boundary conditions.

When approaching to the exit, turbulent kinetic energy increases again, as a result of the acceleration of the axial velocity and the existence of the shear flow caused by the contraction of the combustor geometry.

Both the re-scaled turbulent inflow library condition and the random-fluctuation condition introduce fluctuations in the inflow, with finite turbulent kinetic energy at the inlet. However, the random-fluctuations are damped out quickly. The turbulent kinetic energy falls to the same level as that obtained using the 'laminar inflow' condition within a very short distance. It is seen in Figure 7 that the two inflow conditions, the 'laminar inflow' condition and the random-fluctuation condition give very similar axial distribution of the turbulent kinetic energy, which is consistent with the fact that the two conditions predicted almost identical mean velocity in the flow field. The 're-scaled inflow library' condition also shows a decrease of turbulent kinetic energy in the guiding pipe near the inlet ($x<0$). This is likely due to a mismatch between the 're-scaled inflow turbulence' and the real physical flow and relative coarse grid resolution of wall boundary layers in the guiding pipe. Nevertheless, the decrease rate from the 're-scaled flow library' condition is smaller than that from the other two conditions. Further downstream, turbulent kinetic energy starts to increase, due to the shear layer downstream of the backward-facing step. At the shoulder of the backward-facing step wall ($x=0$) turbulent kinetic energy at the combustor axis reaches its peak value. The sudden decrease of turbulent kinetic energy with the re-scaled inflow library condition in $0<x/H<2$ may be due to the lack of correct shear stresses components, $\langle u'v'\rangle$, $\langle u'w'\rangle$, $\langle v'w'\rangle$, in the inlets.

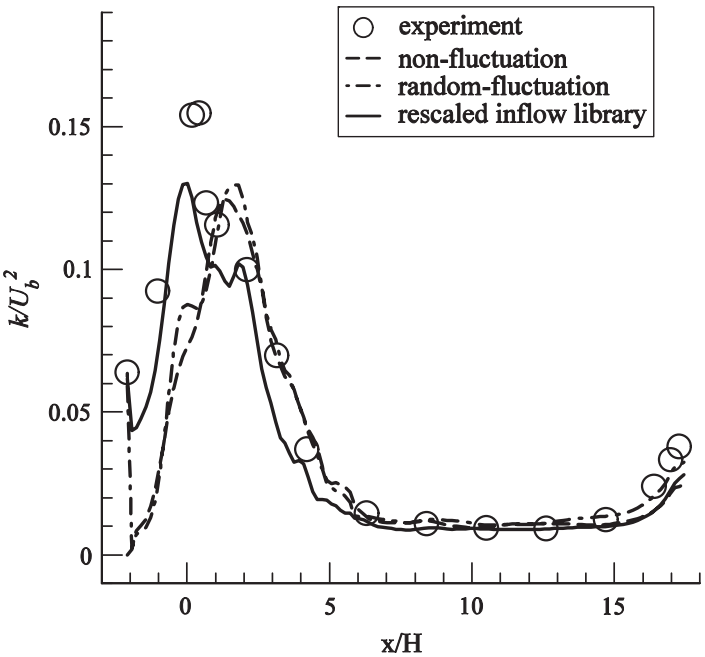

Figure 7. Turbulent kinetic energy distribution along the axis of the dump combustor of test case S43, from the experiment and LES using three different inflow boundary conditions.

Another interesting observation can be made from Figure 7. The peaks of the turbulent kinetic energy calculated with the three inflow conditions do not differ significantly. The decay rates of the turbulent kinetic energy at downstream are also very similar. One may conclude that in turbulent swirling flows, since the production of turbulence is mainly in the shear layers in the IRZ, the inflow turbulence has only a limited effect on the overall turbulence structure in the flow field.

4.2. Influence of inflow swirl velocity profiles

In practical applications, swirl generators may be of many different configurations. Different swirl generators produce different inflow velocity profiles, which may lead to different flow structures in the main combustion chamber. In this section, two different swirl velocity profiles at the inlet are studied and compared to the 'standard case' S43. All the three cases have the same swirl number ($S = 0.43$), the same axial velocity profile, but with different azimuthal velocity profile, as shown in Figure 8. In Case S43A, the peak azimuthal velocity is closer to the pipe wall, and in Case S43B the peak azimuthal velocity is closer to axis of the combustor.

The boundaries of the corner- and the internal recirculation zones, calculated from the time-averaged mean LES data, are shown in Figure 9. It is seen that S43B has the longest IRZ and the earliest vortex breakdown. Case S43A has the shortest IRZ and the latest vortex breakdown. The corner recirculation zone of Case S43A is also shorter than that of Cases S43 and S43B. This can be explained as the following: the radial pressure gradient is proportional to the outward centrifugal force generated by swirling motion, which is $\rho w^2/r$. Since Case

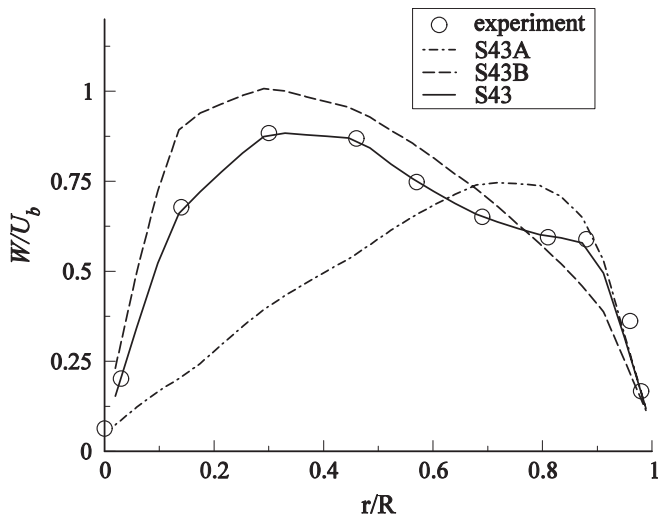

Figure 8. Three inflow swirl velocity profiles with the same axial velocity profile and the same swirl number of $S = 0.43$.

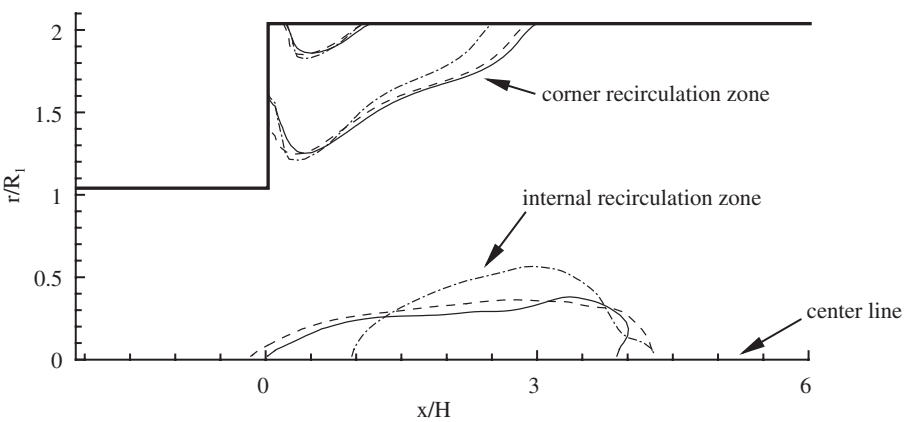

Figure 9. Boundaries of the recirculation zones. Solid line: S43; dashed line: S43B; dot–dashed line: S43A.

S43B has the largest $\rho w^2/r$ near the axis of the combustor, its radial pressure gradient is the highest. This promotes a more favourable axial pressure gradient for the vortex breakdown to occur earlier. Additionally, a higher azimuthal velocity near the outer wall (as in Case S43A) tends to enhance the transport of the axial momentum in the radial direction towards the pipe wall, therefore the reattaching point of the corner recirculation zone is pushed upstream. This underlines the importance of inlet swirl velocity profiles on the control of the vortex breakdown region and the combustion instability.

4.3. Influence of the backward-facing step, outflow conditions and combustor length

In order to assess the influence of the backward-facing step, the outflow conditions and the combustor length, LES of swirling flows in a straight pipe (no backward facing step, no contraction in the pipe), with different pipe lengths, different outflow conditions, are carried out. The diameter of the pipe is $D = 0.1224\,\mathrm{m}$, the inlet bulk velocity is $6.558\,\mathrm{m/s}$, and Re is 21 000. The lengths of the straight pipe are $6D$ and $8D$, respectively. The inlet swirling flow is of solid body rotation type, i.e. the axial velocity is constant across the inlet plane, and the azimuthal velocity varies linearly from zero at the centre to maximum near the wall. To distinguish the influence of swirl intensity, these computations are conducted at two swirl numbers, $S = 0.65$ (Case S65) and $S = 1.8$ (Case S180), respectively.

The two outflow boundary conditions studied here are the zero-gradient outflow condition and the convective outflow condition. Akselvoll and Moin [17] applied a convective outflow boundary condition in the simulation of a confined co-annular jet flow. It was shown that this condition had no visible effect on the flow statistics up to about $1H$ upstream of the exit boundary (H is the height of a backward-facing step).

Figure 10 shows the LES results—the distributions of the swirl number and the mean axial velocity along the axis of the pipe, for the studied eight cases (with two swirl numbers, two pipe lengths, and two outflow conditions, respectively). It is shown that the length of the pipe has little influence on the upstream flow structure. In the low swirl number case ($S = 0.65$, Figure 10(a)) the mean axial velocity is slightly affected in the downstream region, about

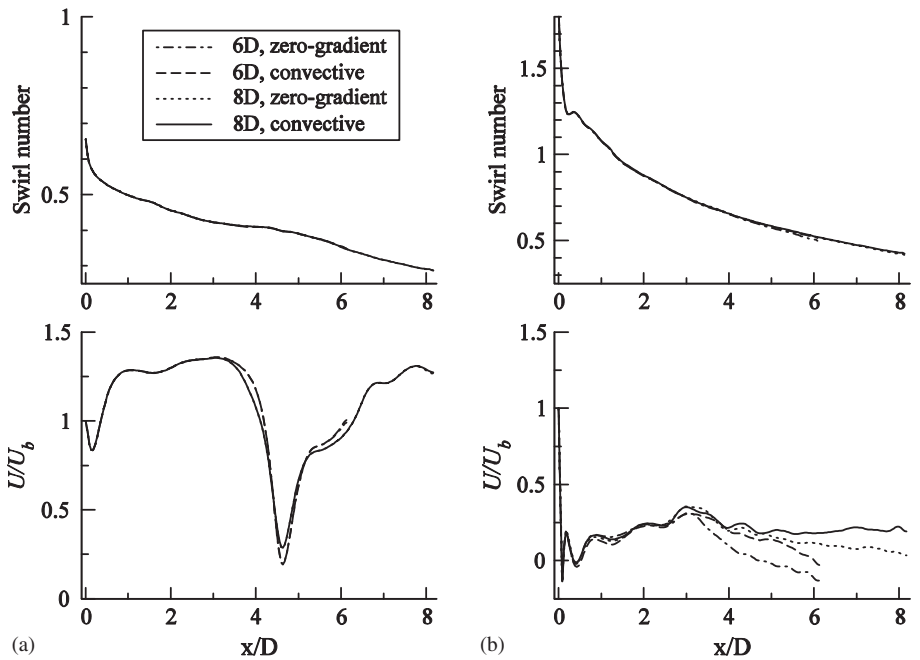

Figure 10. Distribution of the swirl number and the mean axial velocity along the axis of a straight pipe (test cases S65 and S180). Pipe diameter: $D = 0.1224\,\mathrm{m}$; inflow velocity: $U_\mathrm{b} = 6.558\,\mathrm{m/s}$. (a) $S = 0.65$, (b) $S = 1.8$.

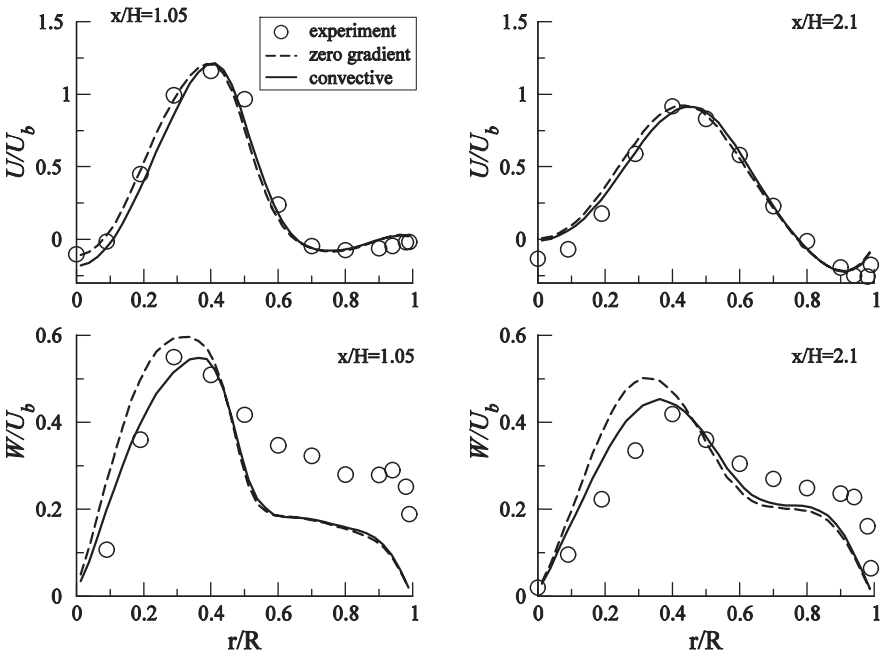

Figure 11. Radial profiles of time-averaged axial and azimuthal velocity components at two axial positions of test case S43, from the experiment and LES using two different outflow boundary conditions.

$3D$ from the outlet. In the high swirl number case ($S = 1.8$, Figure 10(b)) the influence of the pipe length is also limited to the downstream region about $3D$ from the outlet, although the difference in the axial velocity profile is larger than the low swirl case. Figure 10 shows also an important feature of swirling pipe flows—the decay of swirl number along the axial direction. The decay rate of the swirl number is not affected at all by the length of the pipe.

For the low swirl number case ($S = 0.65$, Figure 10(a)), the two outlet conditions predict an identical decay rate of swirl number and an identical mean axial velocity. But for higher swirl number case ($S = 1.8$, Figure 10(b)), the calculated mean axial velocity profiles using two different outflow boundary conditions differ fairly significantly. The difference is larger in the downstream near the outlet. Certain effect of the outflow condition is still evident at $1D$ from the inlet.

The dump combustor case S43 is also simulated with the two outflow conditions. Grid 1 is used, with 2.1 million grid points and without local refinement. The inflow condition is the random-fluctuation superimposed on the measured mean velocity profiles. Mean axial and azimuthal velocity components are plotted in Figure 11. The two outflow conditions predicted a nearly identical axial velocity at the axial positions shown in the figure. However, the azimuthal velocity profiles calculated using different outflow boundary conditions are fairly different. The convective outflow condition predicts a lower peak value of the azimuthal velocity, and gives a result that is a little closer to the experimental data.

The above results suggest that the influence of outflow boundary condition depends strongly on the swirling flow structure itself. For lower swirl number flows without the vortex breakdown, the influence of the outflow condition is very limited. With stronger vortex breakdown,

the influence of the outflow boundary condition can be fairly strong and it affects almost all the flowfield.

It is well known that a higher swirl number leads to an earlier and a stronger vortex breakdown, if the geometry and other flow conditions are kept the same. The swirl numbers of the straight pipe cases are significantly higher than the case with the backward-facing step wall, S43. However, a much weaker vortex breakdown is observed in the straight pipe configuration. In the case $S = 0.65$ no IRZ occurs, as shown in Figure 10(a) (no negative mean axial velocity throughout the whole pipe). In the case $S = 1.8$ (shown in Figure 10(b)), there is only a short region near the inlet where the mean axial velocity has a negative value, indicating a rather weak vortex breakdown. As discussed in the previous section, this is due to the fact that the backward-facing step wall introduces an axial velocity deceleration, which is in favour of the onset of vortex breakdown.

4.4. Influence of the outlet geometry

One may expect that the outlet geometry has an effect on the flow structure as the outflow condition does. To confirm the effect of the outlet geometry, two different outlet configurations are studied. They are the contraction outlet as shown in Figure 1 and a non-contraction outlet. The contraction geometry is the one used in the above computations, Case S43. The non-contraction geometry has an outlet of radius of R_2 (see Figure 1), the same as the combustor radius. The re-scaled turbulent inflow library condition is used in both computations.

Figure 12 shows the mean axial and the azimuthal velocity profiles at two axial positions. As seen, the discrepancy between the two outlet geometries is rather small at these rather

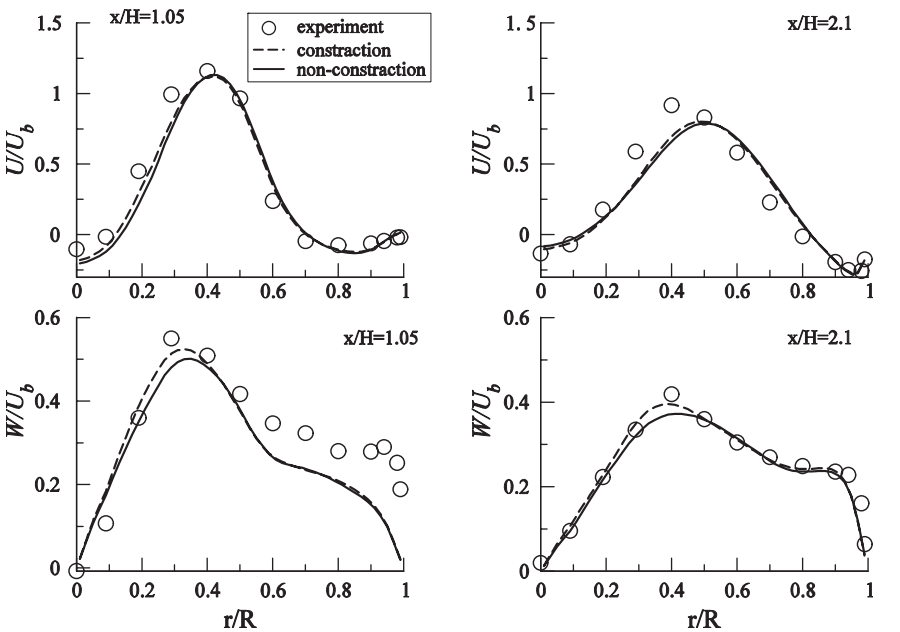

Figure 12. Radial profiles of time-averaged axial and azimuthal velocity components at two axial positions of test case S43, from the experiment and LES using two different outlet geometry configurations.

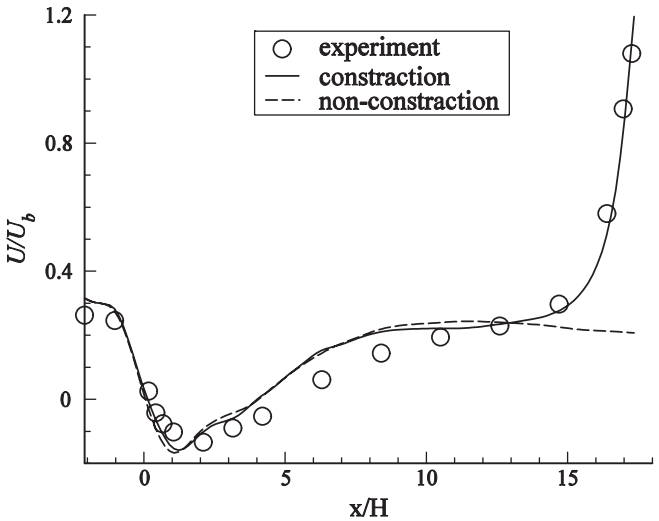

Figure 13. Time-averaged axial velocity component along the axis of the dump combustor of test case S43, from the experiment and LES using two different outlet geometry configurations.

upstream axial positions, particularly in the axial velocity profiles. At far downstream, the effect of the outlet geometry is more noticeable, as seen in the axial velocity variation along the axis of the combustor, shown in Figure 13.

Due to the fact that the outlet area decreases as a result of the geometry contraction, the flow is accelerated quickly at the outlet. As shown in Figure 13, the agreement of the calculated mean axial velocity (with contraction geometry) with the experimental data is good.

4.5. Effect of viscosity

In order to investigate the effects of viscosity on vortex breakdown, a series of swirling flows, with different Reynolds numbers, have been computed. These swirling flows are confined in a circular pipe of radius of 62 mm, and at the inlet there is a sudden axisymmetric contraction. The radius of the inlet is 48 mm. Its geometry is similar to that in Figure 1, with the backward-facing step height about $H/R_1 = 0.29$, and without contraction at the outlet (Case SRE, see Table I). The change of Reynolds number is made by adjusting the molecular viscosity of the fluid, and at the same time, maintaining the inlet velocity profile. Four Reynolds numbers are studied, which are 100, 1000, 10 000, and 100 000, respectively. In order to find out the critical swirl number (at which vortex breakdown starts to occur) at each Reynolds number, flows with different swirl numbers are computed. The inlet swirling flow is of solid body rotation type. The critical swirl number is the swirl number at which the minimum axial velocity along the axis of the pipe is zero.

The minimum axial velocity and the critical swirl number at different Reynolds numbers are shown in Figure 14. It is seen that the minimum axial velocity along the pipe axis decreases monotonously as the swirl number increases. When the swirl number is higher than the critical swirl number, the flow starts to reverse, i.e. vortex breakdown happens. For the case $Re = 100$, the flow is laminar, and the critical swirl number is about 0.66. The critical

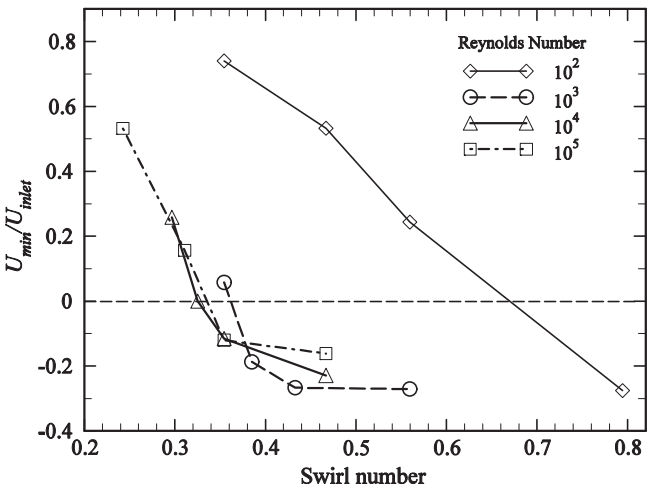

Figure 14. Minimum axial velocity along the central line of test cases SRE at different swirl numbers and Reynolds numbers.

swirl number decreases to 0.36 after increasing Reynolds number to 1000. Increasing Reynolds number even further, the critical swirl number does not change substantially. This is due to the fact that viscous dissipation on the flow kinetic energy is weak at high Reynolds number flows; the flow is easier to develop into the vortex breakdown structure. When the Reynolds number is large enough, the viscosity effect is negligible; the flow and turbulence structures are insensitive to the change of Reynolds number.

One may note that since there is a backward-facing step at the inlet, Case SRE has much lower critical swirl number for the onset of vortex breakdown than the straight pipe cases S65 and S180, although these three cases have the same axial inflow profile (plug flow) and azimuthal velocity profile (solid body rotation). This result confirms again the conclusion of Section 4.3 that vortex breakdown becomes much easy when the backward-facing step exists.

5. CONCLUSIONS

Large eddy simulations of turbulent swirling flows in a model dump combustor are carried out to investigate the flow and turbulence structures, to validate the LES method and to examine the influence of boundary conditions, combustor geometry and Reynolds number on the flow and turbulence structure. High-order finite difference scheme is used based on uniform Cartesian grids and local grid refinements. The sub-grid stress tensor is closed using an SSM model. A high-order wall algorithm is used at the wall boundaries.

Both the time-averaged mean velocity components and the variances of velocity fluctuations obtained from LES are found to be in reasonably good agreement with the corresponding experimental data. Three different inflow boundary conditions are tested, namely, a ‘laminar inflow’ condition, a random fluctuation condition, and re-scaled inflow library condition. The re-scaled inflow library condition has a more physical turbulent kinetic energy spectrum;

thereby it gives more accurate azimuthal velocity profile and better distribution of the turbulent kinetic energy in the flowfield than the other two inflow conditions do. The random fluctuations at the inflow decay rapidly and the results are similar to the results with the 'laminar inflow' condition. Two outflow boundary conditions, a 'zero-gradient' and a 'convective outflow' conditions, are examined. It was shown that the latter condition yields better results. The outflow conditions affect the results mostly at downstream region near the outlet; however, at very high swirl numbers the effect of the outflow condition can be evident in the whole flowfield.

LES results show that turbulence in the dump combustor is highly anisotropic, in particular in the upstream immediately behind the backward-facing step wall. Turbulence is generated in two shear layers. One is at the shoulder of the backward-facing step wall, where high shear exists and the flow instability of Kelvin–Helmholtz type occurs. The second shear layer is near the axis of the combustor where an internal recirculation zone exists as a result of the vortex breakdown. Along the axial direction downstream, turbulence becomes more isotropic and decays quickly.

The onset of vortex breakdown is not very sensitive to the combustor length and the outlet configuration, but very sensitive to the sudden expansion at the inlet. Without the backward-facing step at the inlet, much higher swirl number is needed for the vortex breakdown to occur. The inflow swirl generator (and thus the inflow azimuthal velocity profile) is found to be influential on the size and the position of the internal recirculation zone. For low Reynolds number laminar flows, increasing Reynolds number leads to a lower critical swirl number, due to the decrease of viscous dissipation of kinetic energy. However, once the Reynolds number is high enough, the swirling flow and turbulence structure are not sensitive to the change of Reynolds number.

NOMENCLATURE

E	Eulerian energy time spectrum (m^2/s)
G	LES filter function (m^{-3})
H	height of the backward-facing step (m)
P	pressure (Pa)
R_1, R_2	radius of the combustor (m)
Re_l	turbulent Reynolds number (non-dimensional)
S	swirl number (non-dimensional)
U, V, W	mean velocity in axial, radial, and azimuthal direction (m/s)
U_b	inlet bulk velocity (m/s)
U_con	mean outflow velocity (m/s)
f	frequency (s^{-1})
k	turbulent kinetic energy (m^2/s^2)
l	integral length scale (m)
n	normal direction to the outlet plane
u, v, w	instantaneous velocity components in axial, radial, azimuthal directions (m/s)
u_i	velocity components in Cartesian co-ordinate x_i directions (m/s)
u', v', w'	velocity fluctuation (m/s)

$\langle u'u' \rangle, \langle w'w' \rangle, \langle u'v' \rangle, \langle u'w' \rangle, \langle v'w' \rangle$	Reynolds stresses (m^2/s^2)
x_i	Cartesian co-ordinates (m)

Greek letters

Δ	LES filter width (m)
$\hat{\Delta}$	filter width of the second filter (m)
δ_{ij}	Kronecker delta
ε	dissipation rate of k (m^2/s^3)
$\bar{\phi}$	filtered flow variable of ϕ in LES
$\hat{\phi}$	filtered flow variable of ϕ with the second filter function
λ	Taylor micro length scale (m)
ν	kinematic viscosity (m^2/s)
ρ	density (kg/m^3)
τ_{ij}	sub-grid scale (SGS) stress tensor (m^2/s^2)

ACKNOWLEDGEMENTS

This work has been supported by the Swedish Research Council (VR), and partially supported by the Center for Combustion Science and Technology (CeCOST) and the National Supercomputer Center (NSC) in Linköping, Sweden.

REFERENCES

1. Billant P, Chomaz JM, Huerre P. Experimental study of vortex breakdown in swirling jets. *Journal of Fluid Mechanics* 1998; **376**:183–219.
2. Panda J, Mclaughlin DK. Experiments on the instabilities of a swirling jet. *Physics of Fluids* 1994; **6**:263–276.
3. Wang S, Rusak Z. On the stability of an axisymmetric rotating flow in a pipe. *Physics of Fluids* 1996; **8**: 1007–1016.
4. Fernandez-Feria R, Ortega-Casanova J. Inviscid vortex breakdown models in pipes. *Zeitschrift für angewandte Mathematik und Physik* 1999; **50**:698–730.
5. Kubo I, Gouldin FC. Numerical calculations of turbulent swirling flow. *Journal of Fluids Engineering—Transactions of ASME* 1975; **97**:310–315.
6. Nejad AS, Vanka SP, Favaloro SC. Application of laser velocimetry for characterization of confined swirling flow. *Journal of Engineering for Gas Turbines and Power* 1989; **111**:36–45.
7. Weber R, Visser BM, Boysan F. Assessment of turbulence modeling for engineering prediction of swirling vortices in the near burner zone. *International Journal of Heat and Fluid Flows* 1990; **11**:225–235.
8. Schmittel P, Gunther B, Lenze B, Leuchel W, Bochhorn H. Turbulent swirling flames: experimental investigation of the flowfield and formation of nitrogen oxide. *Proceedings of the Combustion Institute* 2000; **28**:303–309.
9. Lu P, Semião V. A new second-moment closure approach for turbulent swirling confined flows. *International Journal for Numerical Methods in Fluids* 2003; **41**:133–150.
10. Lucca-Negro O, O'Doherty T. Vortex breakdown: a review. *Progress in Energy and Combustion Science* 2001; **27**:431–481.
11. Piomelli U. Large-eddy simulation: achievements and challenges. *Progress in Aerospace Sciences* 1999; **35**: 335–362.
12. Pierce CD, Moin P. Large eddy simulation of a confined coaxial jet with swirl and heat release. *AIAA* 98-2892, 1998.
13. Kim WW, Menon S, Mongia HC. Large eddy simulation of a gas turbine combustor flow. *Combustion Science and Technologies* 1999; **143**:25–62.
14. Klein M, Sadiki A, Janicka J. A digital filter based generation of inflow data for spatially developing direct numerical or large eddy simulations. *Journal of Computational Physics* 2003; **186**:652–665.

15. Lund TS, Wu X, Squires KD. Generation of turbulent inflow data for spatially-developing boundary layer simulations. *Journal of Computational Physics* 1998; **140**:233–258.
16. Spalart PR. Direct numerical simulations of a turbulent boundary layer up to $Re_\theta = 1410$. *Journal of Fluid Mechanics* 1988; **187**:61–98.
17. Akselvoll K, Moin P. Large-eddy simulation of turbulent confined coannular jets. *Journal of Fluid Mechanics* 1996; **315**:387–411.
18. Pauley LL, Moin P, Reynolds WC. The structure of two-dimensional separation. *Journal of Fluid Mechanics* 1990; **220**:397–411.
19. Gullbrand J, Bai XS, Fuchs L. High-order Cartesian grid method for calculation of incompressible turbulent flows. *International Journal for Numerical Methods in Fluids* 2001; **36**:687–709.
20. Smagorinsky J. General circulation experiments with the primitive equations. *Monthly Weather Review* 1963; **91**:99–152.
21. Liu S, Meneveau C, Katz J. On the properties of similarity subgrid scale models as deduced from measurements in a turbulent jet. *Journal of Fluid Mechanics* 1994; **275**:83–119.
22. Wang P, Bai XS, Wessman M, Klingmann J. Large eddy simulation and experimental studies of a confined turbulent swirling flow. *Physics of Fluids* 2004; **16**:3306–3324.
23. Pierce CD. Progress-variable approach for large eddy simulation of turbulent combustion. *Ph.D. Dissertation*, Stanford University, U.S.A., June, 2001.
24. Pierce CD, Moin P. Method for generating equilibrium swirling inflow conditions. *AIAA Journal* 1998; **36**: 1325–1327.

